ACSNANO

www.acsnano.org

ARTICLE

Simultaneous Characterization of In-Plane and Cross-Plane Resistivities in Highly Anisotropic 2D Layered Heterostructures

Sizhe Weng, Yu Wang, Celsey Price, Hannah R. Blackwood, Marisa Choffel, Aaron Miller, Ruoxi Li, Mingrui Chen, Ping Lu, Sina Ilkhani, Arun Majumdar, David C. Johnson,* and Stephen B. Cronin*

Cite This: https://doi.org/10.1021/acsnano.3c13232

Read Online

ACCESS | Metrics & More | Article Recommendations | Supporting Information

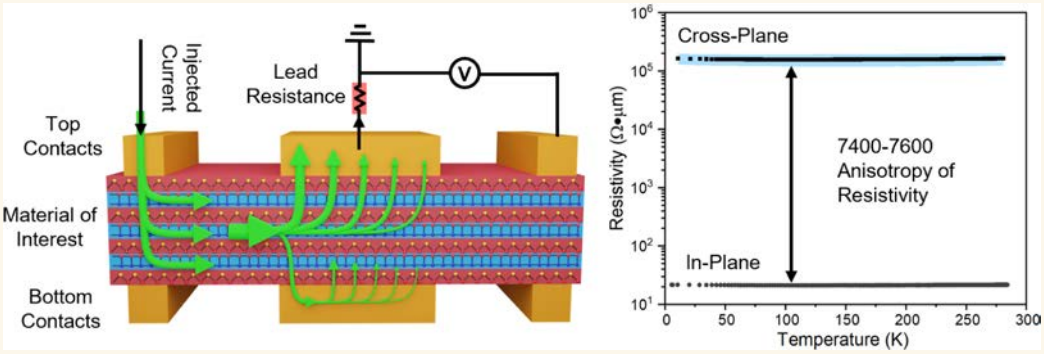

ABSTRACT: **Understanding and characterizing the intrinsic properties of charge carrier transport across the interfaces in van der Waals heterostructures is critical to their applications in modern electronics, thermoelectrics, and optoelectronics. However, there are very few published cross-plane resistivity measurements of thin samples because these inherently 2-probe measurements must be corrected for contact and lead resistances. Here, we present a method to extract contact resistances and metal lead resistances by fitting the width dependence of the contact end voltages of top and bottom electrodes of different contact widths to a model based on current crowding. These contributions are then subtracted from the total 2-probe cross-plane resistance to obtain the cross-plane resistance of the material itself without needing multiple devices and/or etching steps. This approach was used to measure cross-plane resistivities of a $(PbSe)_1(VSe_2)_1$ heterostructure containing alternating layers of PbSe and VSe_2 with random in-plane rotational disorder. Several samples measured exhibited a 4 order of magnitude difference between cross-plane and in-plane resistivities over the 6−300 K temperature range. We also reported the observation of charge density wave transition in the cross-plane transport of the $(PbSe)_1(VSe_2)_1$ heterostructure. The device fabrication process is fully liftoff compatible, and the method developed enables the straightforward measurement of the resistivity anisotropy of most thin film materials with nm thicknesses.**

KEYWORDS: *anisotropy, resistivity, characterization, contact resistance, van der Waals heterostructures*

INTRODUCTION

Semiconducting heterostructures and superlattices have attracted considerable interest in the scientific and industrial communities due to their exotic properties and wide range of applications in modern electronics, thermoelectrics, and optoelectronics.[1−4] Early studies focused on III−V semiconducting heterostructures and oxide superlattices, which were mainly fabricated through epitaxial growth, such as molecular beam epitaxy (MBE)[5,6] or metal organic chemical vapor deposition (MOCVD).[7,8] Although many state-of-the-art electronic devices (i.e., photodetectors and light-emitting diodes) have been demonstrated, such growth methods are constrained by crystallographic symmetry similarities and lattice constant matching. More recently, van der Waals (vdW) heterostructures with vertical integration of layered

Received: December 31, 2023
Revised: August 20, 2024
Accepted: August 21, 2024

materials offer an alternative approach to integrate two-dimensional materials that do not rely on strong chemical bonding between adjacent layers.[1,9] Such heterointegration provides a more versatile selection of materials with disparate lattice structures, such as graphene, hexagonal boron nitride (hBN), and transition metal dichalcogenides (TMDs).[10] The optical and electrical properties of vdW heterostructures and devices have been under intensive study, and many interesting phenomena have been discovered, including ultrafast charge transfer (within 50 fs) in photoexcited MoS_2/WS_2 heterostructures, 55% external quantum efficiency of photocurrent generation in graphene/MoS_2/graphene vertical junctions,[11,12] all-electrical single photon light emitting diodes realized in graphene/hBN/WS_2 heterostructures,[13] and graphene/hBN/graphene field effect tunneling transistors.[14] Recently, there has been a emerging trend in vertically integrating 2D materials with traditional semiconductors and oxide superlattices, resulting in the creation of even more exotic artificial heterostructures or superlattices with atomically clean and electronically distinct interfaces.[15,16] Since the functionalities of most of the above-mentioned heterostructures and superlattices rely heavily on the carrier transport across the interfaces, studying the fundamental electrical transport properties in the cross-plane direction of vdW heterostructures is of great importance to the future development of nanoelectronics and nanophotonics.

There are few reports probing the intrinsic properties of charge carrier transport across the interfaces in vdW heterostructures due to the difficulty of separating large contact resistances from the relatively small cross-plane resistance of thin films (1−100 nm thick) in 2-probe measurements. The most common method of measuring resistivity tensors in anisotropic materials is based on the method developed by Montgomery.[17] However, their approach requires the contact width of the contacts to be less than 10% of the film thickness to measure the cross-plane resistivity accurately.[18] For 50 nm thick vdW heterostructures, it is very difficult to fabricate Ohmic metal contacts with contact widths smaller than 5 nm. Another approach used to extract the resistivity in the cross-plane direction include measuring properties in samples where regions between contact pads have been etched to varying depths to form a mesa structure, followed by applying the modified transfer line method (M-TLM).[3,19−21] These methods require the variation of contact resistance between different devices to be much smaller than the cross-plane resistance of the material, which is challenging to achieve experimentally for a variety of reasons including surface damage from contact metal deposition, Fermi level pinning, and nonuniformity at the material/contact interface.[22,23] Another reported approach is to sandwich the material of interest between a large bottom electrode and a small top electrode in a two-probe measurement configuration.[24] However, the measured resistance includes the lead and contact resistance from the metal/material interface, which usually dominates in the measured total resistance in the cross-plane direction.

The approach to measure cross plane resistivity presented in this paper is based on the phenomena of current crowding, which was extensively explored in the 1960s and 1970s.[25−27] The phenomenon of current crowding has been shown to be very important in diverse areas, ranging from being an important loss mechanism in LED's[28] to increasing electromigration leading to the formation of interfacial voids.[29] Figure 1 illustrates the basis of current crowding using a transition line model where magenta resistors represent the interface resistance. Current flowing from the yellow to the green wires will not be the same in each of the intervening magenta resistors. More current will pass through the initial resistor than later ones, with the amount dependent on the resistivities of both the wires and the interface. To measure cross plane resistivity, we need to add contacts on the bottom of the sample, which adds a second interface and potential current pathway through the contact and across to the opposite contact. The transmission line model derived herein includes the bottom contact, which modifies the top current distribution if the in-plane conductivity is low.

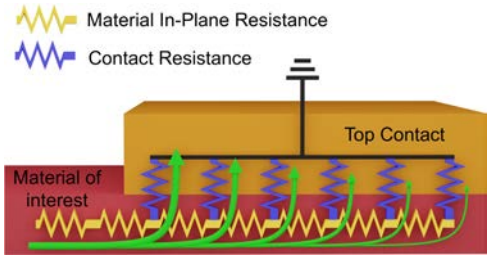

Figure 1. Schematic diagram of an equivalent circuit illustrating the concept of current crowding. More current flowing from the yellow to the black wires will pass through the initial intervening blue resistors than later ones, with the amount dependent on the resistivities of both the material of interest and the interface.

Here, we present a approach to characterize both the in-plane and cross-plane resistivities of ultrathin samples. We use in-plane measurements to determine the resistances of the lithographically defined gold leads connecting the sample to the bonding pads (typically 20−100 Ω) and the contact resistivities of the top and bottom contacts. These contributions are then subtracted from the measured two-probe total cross-plane resistance to obtain the cross-plane resistance of the heterostructure material. The cross-plane resistivity is calculated from the cross-plane resistance using the measured sample thickness and contact areas. This approach uses a simple device geometry without needing multiple devices and/or etch steps. We demonstrate the utility of our approach by characterizing several $(PbSe)_1(VSe_2)_1$ heterostructures, all yielding 4 order of magnitude anisotropies between the in- and out-of-plane resistivities over the 6−300 K temperature range. In this work, the electrical properties of nm thick van der Waals heterostructures have been characterized in both directions on the same device with contact resistances fully accounted for, and we believe this technique can be generalized and applied to characterize a wide range of thin film materials if the deposition or growth of the target material does not require epitaxial substrates.

RESULTS AND DISCUSSION

The optical image and schematic diagram of as-fabricated device are shown in Figure 2a,b. In the present study, 50 unit cells of the $(PbSe)_1(VSe_2)_1$ heterostructure (~30 nm thick) are sandwiched between arrays of top and bottom electrodes with 5 contact widths ranging from 1 to 16 μm, detailed fabrication processes are demonstrated in the Method section. Figure 3a−c shows the characterization data obtained on an annealed $(PbSe)_1(VSe_2)_1$ heterostructure using the conditions

https://doi.org/10.1021/acsnano.3c13232
ACS Nano XXXX, XXX, XXX−XXX

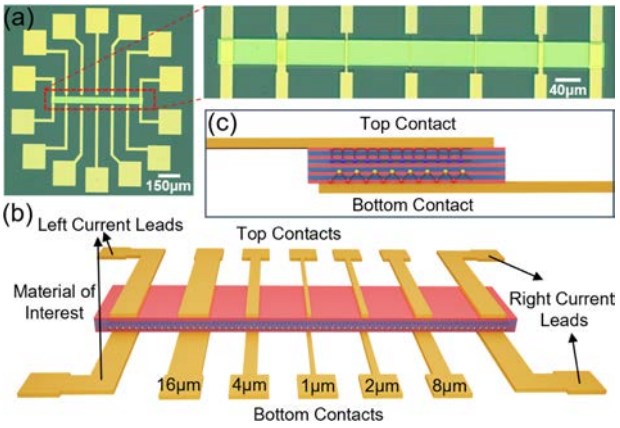

Figure 2. (a) Optical microscope image and (b) schematic diagram of the as-fabricated device with various contact widths from 1 to 16 μm. (c) Side view of the device, shows that the top and bottom electrodes extend across the material of interest. The electrodes end at 3 μm away from the edge of the material to avoid potential short circuit between top and bottom contacts.

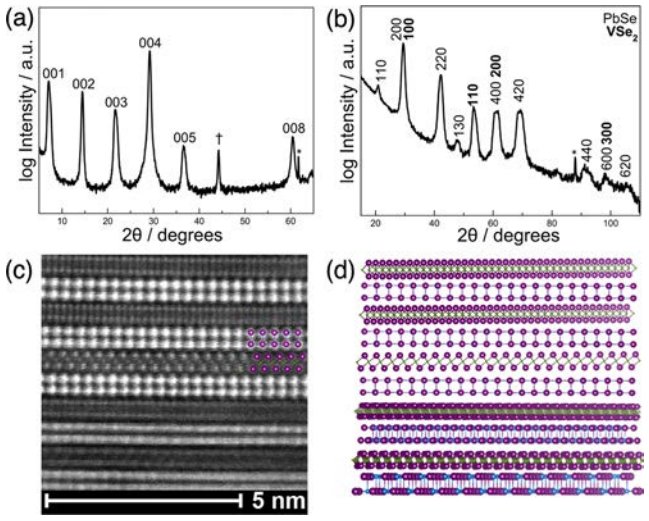

Figure 3. (a) The specular diffraction pattern of a $(PbSe)_1(VSe_2)_1$ heterostructure. The indices are given above each reflection. (b) Grazing incidence in plane X-ray diffraction patterns of the self-assembled $(PbSe)_1(VSe_2)_1$ heterostructure collected from a sample subjected to identical annealing conditions as the fabricated device. Indices for both the PbSe and VSe_2 sublattices are given above each reflection. (c) High angle annular dark field scanning tunneling electron microscopy (HAADF-STEM) image of $(PbSe)_1(VSe_2)_1$ heterostructure. Colored bars show the positions of atomic planes of Pb (blue), V (green), and Se (purple). (d) A schematic of the structure of the $(PbSe)_1(VSe_2)_1$ heterostructure illustrating the off-axis rotational disorder of the constituent sublattices seen in the HAADF-STEM image.

described above. These data show the formation of highly crystalline materials with atomically sharp interfaces.

The completed devices are used to measure the in-plane resistivity of the material of interest using a 4-probe configuration to make sure the processing steps have not altered the properties of deposited film. We used 4 top or bottom contacts to perform a 4-probe in-plane transport measurement, in which the current is flowing between the two outer electrodes and the voltage difference between the 1 and 2 μm leads was measured. At each temperature, the conducting current increases from −0.2 to 0.2 mA in 50 μA incremental steps and Ohmic behavior is observed. The temperature dependent corrected in-plane resistivity, plotted in Figure S6a. Figure S6c shows a similar order of magnitude and temperature dependence to that previously reported by Wang et al.,[30] Hite et al.,[31] and Cordova et al.[32] The upturn in the resistivity at low temperatures results from a charge density wave transition in the monolayer thick VSe_2 layers.[33] The in-plane resistivity data indicate that the $(PbSe)_1(VSe_2)_1$ heterostructure survived the processing steps.

A sequence of 2-probe in-plane measurements using the top and bottom contacts are then conducted to determine the lead and contact resistances, as illustrated in Figure 4a. Current is injected through pairs of contacts, and the voltage of an adjacent contact is measured relative to ground. Typical I−V curves for the 2-probe measurements are plotted in Figure S1 showing Ohmic behavior at the metal/heterostructure interface. The measured voltage is the sum of the potential drop due to the current flowing through the lithographically defined electrode connecting the heterostructure material to the bonding pads (i.e., leads) and the voltage drop at the end of the contact due to the fraction of the total current (1 mA) flowing through the end of the contact. This latter contribute is referred to as the contact end voltage. The amount of current flowing through the far end of the grounded contact depends on the contact width of the contact and the relative magnitude of the contact conductance with respect to the sample's in-plane resistivity, resulting in the systematic trend in the measured voltage with contact width plotted in Figure 5a. The fits to these contact width-dependent curves are described below.

Figure 4b presents a schematic illustration of the theoretical analysis of the in-plane current flowing through a contact. Here, $V_{top}(x)$ and $V_{bottom}(x)$ are the electrical potential differences between the material and the top and bottom contacts as a function of position x, measured from the inner edge of the contact. The contact resistances are modeled by adding parallel resistors on both the top and bottom of the material, and G'_{top} and G'_{bottom} represent the conductances of the interface per unit length of the top and bottom contacts, respectively.[34] We assume the contact is at an equal potential as a function of position, x, since the resistivity of the contact material (Au) is around 10^{-8} Ω·m,[31−35] which is very small comparing with the in-plane resistivity of the $(PbSe)_1(VSe_2)_1$ heterostructure. $I(x)$ represents the current flowing in the material at location x along the contact and R', the in-plane material resistance per unit length, is taken as a constant at each measurement temperature (21.8 $\Omega\cdot\mu m^{-1}$ at room temperature) calculated from the in plane 4-probe resistivity measurement. The top contact is grounded while the bottom contact is floating. Then, $V_{top}(x)$, $V_{bottom}(x)$, and $I(x)$ can be analyzed by constructing the following differential equations:

$$\frac{dV_{top}(x)}{dx} = -R'I(x) \quad (1)$$

$$\frac{dV_{bottom}(x)}{dx} = -R'I(x) \quad (2)$$

$$\frac{dI(x)}{dx} = -G'_{top}V_{top}(x) - G'_{bottom}V_{bottom}(x) \quad (3)$$

https://doi.org/10.1021/acsnano.3c13232
ACS Nano XXXX, XXX, XXX−XXX

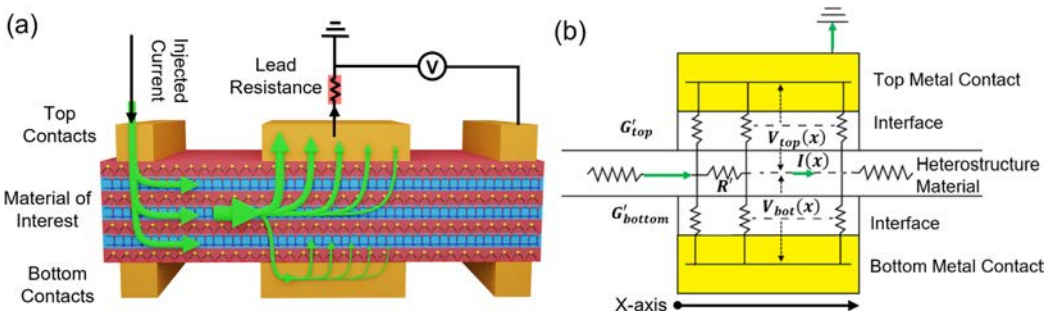

Figure 4. (a) Schematic diagram of the three-terminal voltage measurement showing the nonuniform current distribution in the grounded top contact and the floating bottom contact. The voltage measured is the sum of the voltage drop at the end of the top contact due to the current density there and the voltage drop across the lithographically defined gold lead connecting the material of interest to the bonding pad. The current distribution in the floating bottom contact also indicates the significance of the impact from the bottom electrode, even if only the top electrodes are being measured. (b) Equivalent circuit diagram of the in-plane and cross-plane current flow analysis. The positive x direction and the origin of the axis are indicated at the bottom.

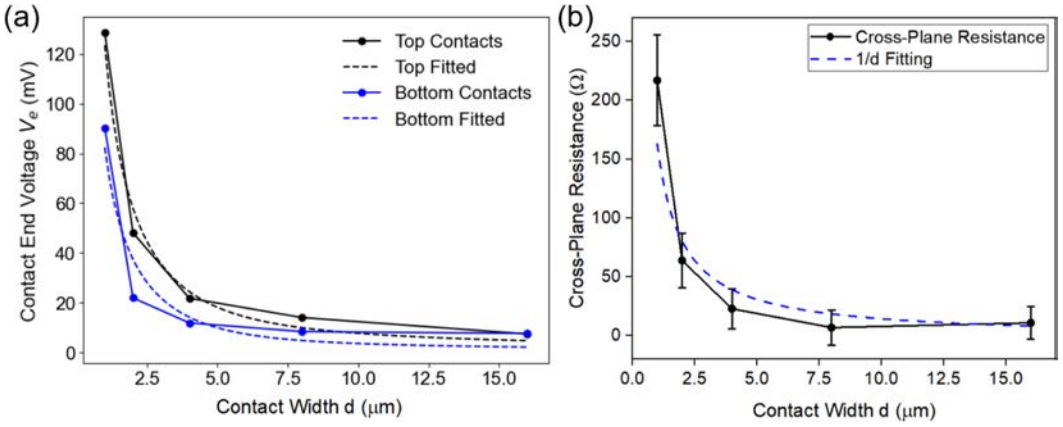

Figure 5. (a) The measured voltage drop plotted as a function of the contact width. As the contact width becomes larger, the current density at the end of the contact approaches zero, and the measured voltage approaches the voltage drop due to the gold lead connecting the material of interest to the bonding pad. (b) The contact-subtracted cross-plane resistance plotted as a function of contact width. Since the contact lengths (perpendicular to the direction of current flow) are all equal, the resistance should vary as 1/d. The blue curve is the best fit through the data points.

The equations are solved by applying Dirichlet and integral form boundary conditions: $I(x = 0) = Ii$, $I(x = d) = 0$, and $\int_0^d G'_{top} V_{top}(x) = I_i$, where $I_i$is the total current in the material before entering the region between the contacts, and d is the contact width. Based on the above-mentioned constraints, the solutions are as follows:

$$V_{top}(x) = ZI_i \coth(\alpha d)\cosh(\alpha x) - ZI_i \sinh(\alpha x) + \frac{G'_{bottom}}{G'_{top}} \frac{I_i}{(G'_{top} + G'_{bottom})d} \quad (4)$$

$$V_{bottom}(x) = ZI_i \coth(\alpha d)\cosh(\alpha x) - ZI_i \sinh(\alpha x) - \frac{I_i}{(G'_{top} + G'_{bottom})d} \quad (5)$$

$$I(x) = I_i \cosh(\alpha x) - I_i \coth(\alpha d)\sinh(\alpha x) \quad (6)$$

where $Z = \sqrt{\frac{R'}{(G'_{top} + G'_{bottom})}}$ and $\alpha = \sqrt{(G'_{top} + G'_{bottom})R'}$. This result is similar to previous analyses for a single top contact in which the potential difference between the material and contact also follows hyperbolic decay along the contact periphery.[34,36,37] However, for our top and bottom contact configuration, the voltage drop across the material/contact interface contains an additional term containing the contact width d and the conductance of both top and bottom contacts. We define the contact end voltage drop as[22]

$$V_{end} = V(x = d) \quad (6.5)$$

During the experiment, top contacts are first grounded to measure V_{end}^{top} followed by bottom electrodes grounded to study V_{end}^{bot} with the definitions given by

$$V_{end}^{top} = \frac{ZI_i}{\sinh(\alpha d)} + \frac{G'_{bottom}}{G'_{top}} \frac{I_i}{(G'_{top} + G'_{bottom})d} + R_{lead}^{top} I_i \quad (7)$$

$$V_{end}^{bot} = \frac{ZI_i}{\sinh(\alpha d)} + \frac{G'_{top}}{G'_{bottom}} \frac{I_i}{(G'_{top} + G'_{bottom})d} + R_{lead}^{bottom} I_i \quad (8)$$

where R_{lead}^{top} and R_{lead}^{bottom} represent the contact lead resistances of the top and bottom electrodes, respectively. Figure 5a shows the contact end voltage measurements plotted with respect to contact width and the results of fitting this data to eqs 7 and 8. The theoretical analysis fits the data well, indicating that the

https://doi.org/10.1021/acsnano.3c13232
ACS Nano XXXX, XXX, XXX−XXX

floating contact on the other side must be included as it provides a parallel pathway for the current. The extracted contact lead resistivities per unit length ρ_{lead}^{top} and ρ_{lead}^{bottom} are 2.42 ± 0.16 and 0.85 ± 0.16 Ω·μm^{-1}, respectively. The fitted values of G'_{top} and G'_{bottom} are (7.91 ± 0.72) × 10^{-3} and (11.7 ± 1.6) × 10^{-3} Ω^{-1}·μm^{-1}, resulting in contact resistivities of (5.1 ± 0.6) × 10^3 and (3.4 ± 0.6) × 10^3 Ω·μm^2 for the top and bottom contacts, respectively. These values are on the same order of magnitude as that of Au/WSe_2 interface reported previously.[38]

The cross-plane resistances were measured between top and bottom contact pairs with different contact widths. The measured resistance is the sum of the two contact resistances (determined from G'_{top} and G'_{bottom}), the two contact leads resistances (R_{lead}^{top} and R_{lead}^{bottom}), and the cross-plane resistance of the material itself. Figure 5b presents the extracted cross-plane resistances plotted with respect to the contact width. Since the width of the contacts in the other dimension (perpendicular to the current flow) is kept constant (i.e., 40 μm), one would expect the extracted material cross-plane resistance to vary as 1/d if the current is confined to the area of the contact as it crosses the sample, which is shown as the fitted line in Figure 5b. While there is considerable error, mainly due to taking the difference of two large numbers, the systematic 1/d trend in resistance with contact width indicates the uniformity of both the top and bottom contacts across the sample. The fitted average cross-plane resistivity from this simple model is 160,000 ± 50,000 Ω·μm, which is 4 orders of magnitude larger than the measured in-plane resistivity.

A potential source of systematic error in converting the cross-plane resistance into a resistivity lies in assuming that the cross-sectional area is equal to the contact dimensions. Depending on the sample resistivity and thickness, there will be broadening of the flowing pathway of the injected current in the sample after passing through the contacts. This effect becomes especially important as the contact widths become smaller and/or the sample becomes thicker. There is an inherent trade-off in choosing the contact widths. The impact of lateral current spreading is smaller as contact widths are increased. However, larger contact widths result in smaller cross-plane resistances, which results in larger uncertainties after the large contact and lead resistances are subtracted from the measured total cross-plane resistance. Smaller contact widths give larger cross-plane resistances after the contact and lead resistances are subtracted from the measured cross-plane resistance. However, current spreading needs to be considered when converting the resistances to cross-plane resistivities. In the sample studied, the impact of lateral current spreading is small as evidenced by the observed 1/d dependence of contact resistance versus contact width in Figure 5b. Figure S2 contains simulations of current spreading as functions of sample thicknesses and contact widths, which also shows small current broadening effect when sample thickness is in tens of nanometers.

We measured the temperature dependent on the cross-plane resistivity through the 1 and 2 μm leads to probe possible mechanisms for the very large difference between the in plane and cross plane resistivities. Considering the experimental trade-offs discussed above, the relatively small contact areas of the 1 and 2 μm widths maximize the sample cross-plane resistance, which is advantageous when subtracting the interface and lead resistances from the total measured cross plane resistance. We measured the systematic change in the contact end voltage with contact width at six different temperatures, which were used to determine the contact conductances and lead resistances at each temperature (see Figure S3 for the fits of the contact end voltages). The change in the lead resistances with temperature (Figure 6b) are

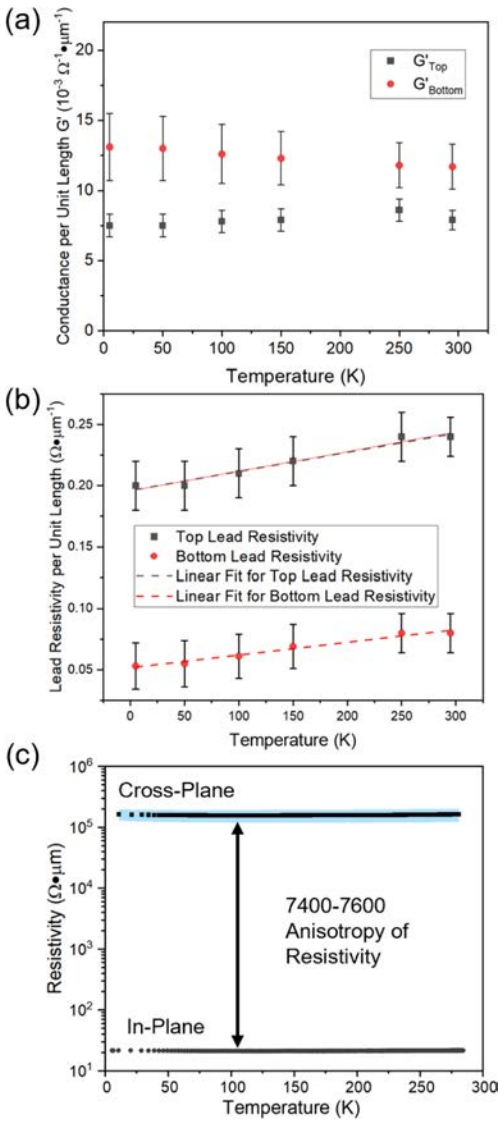

Figure 6. Temperature dependence of (a) interface contact conductance per unit length, and (b) subtracted lead resistivity per unit length of top and bottom electrodes. (c) Extracted cross-plane and in-plane resistivities of $(PbSe)_1(VSe_2)_1$ heterostructure plotted with respect to temperature.

consistent with the expected temperature dependence of the metallic gold leads.[39,40] Within the experimental error, the measured contact conductances are temperature independent (Figure 6a).

Despite their importance in electromechanical devices, there are surprisingly few reports of large area contact conductances because of the strong dependence of interface conductance on surface roughness, contamination, and other nonuniformities. The difficulties in reproducibly preparing interfaces make measurement of intrinsic interface resistances challenging. A

https://doi.org/10.1021/acsnano.3c13232
ACS Nano XXXX, XXX, XXX−XXX

recently reported island size dependent electrical contact resistance of nanoscale gold islands on graphite with atomically flat interfaces using conductive atomic force microscopy showed that the total measured resistance is the sum of the resistances between the tip and the gold and the gold and the graphite, which were challenging to separate.[41] The temperature independent conductance values we observed are reasonable, given the metallic nature of the gold contacts and VSe_2 surface layers of our heterostructure.

The temperature dependent measurement of both cross-plane and in-plane material resistivities is plotted in Figure 6c. The resistivity in the cross-plane direction with 2 μm width shows a value of around 160,000 $\Omega\cdot\mu$m throughout the entire temperature range, decreasing smoothly by about 5% to a minimum value at ~100 K before increasing by the same amount as the temperature is decreased to 6 K (Figure S6b). The temperature dependence is very similar to the measured in plane resistivity, which has a minimum resistivity at a similar temperature that is 2% smaller than the room temperature value. This indicates that the charge density wave transition is also observed in the cross-plane transport of $(PbSe)_1(VSe_2)_1$ heterostructure, which has not been reported before. The net result is that ratio of the cross-plane resistivity divided by the in-plane resistivity is relatively constant as a function of temperature, varying between 7400 and 7600.

Previous studies have shown similar high anisotropy between the resistivity along the *c*-axis and *a*-axis in bulk highly oriented pyrolytic graphite (HOPG), and they attributed the conducting mechanism in the cross-plane direction to thermal excitation of charge carriers across stacking fault potential barriers as well as impurity-assisted interlayer hopping.[42] This leads to nonlinear $I-V$ curves, which are also reported in cross-plane studies of $NbSe_2$ and HfS_2 multilayer flakes.[24] High resistivity anisotropy has also been observed in In_2Se_3 nanowires, in which semiconducting and metallic behaviors are observed along different crystal directions.[43] However, all the findings mentioned above only involve single component materials. For vdW heterostructures, the anisotropy is mostly attributed to the weekly interacting van der Waals gap between two adjacent layers.[21,24,44] Kwon et al. have reported an anisotropy of 2000 from Sb_2Te_3/GeTe superlattice films.[21] These values are similar to our measured anisotropy.

The four-order-of-magnitude ratio of cross-plane to in-plane resistivity found for $(PbSe)_1(VSe_2)_1$ heterostructure in our study is of similar magnitude to previous reports for misfit layer compounds. Misfit layer compounds are a family of materials containing transition metal dichalcogenide layers interleaved with rock salt structured layers $(MX)_{1+d}TX_2$ where M is Sn, Pb, Bi or a rare earth metal, X is S or Se, d is the misfit parameter determined for the ratio of unit cell areas of the two constituents and T is Ti, V, Nb or Ta. The $(PbSe)_1(VSe_2)_1$ investigated in this work differs from a misfit layer compound by having turbostratic disorder between the PbSe and VSe_2 planes. Prior reports of anisotropy of electrical resistivity of misfit layer compounds ranged from factors of 50 to 10,000 depending on the compound investigated.[45] Our measured anisotropy falls within the range previously reported. The only report of the temperature dependence of the anisotropy of a misfit layer compound, $(SnS)_{1.17}NbS_2$, was also temperature independent.[41] Both $(SnS)_{1.17}NbS_2$ and $(PbSe)_1(VSe_2)_1$ consists of a structural layer that is a small bandgap semiconductor as a bulk phase (SnSe or PbSe) and alternating with a transition metal dichalcogenide which is metallic as a bulk phase (NbS_2 or VSe_2). One would expect the cross-plane transport to be dominated by the small band gap semiconductor while the in-plane transport to be dominated by the metallic layer. For alternating thick layers of these materials, one would expect a temperature dependent anisotropy due to the temperature dependent carrier concentration of the semiconducting layer. The similar temperature dependences of the in-plane and cross-plane resistivities of our data suggest both conductivities are related to the density of states of the VSe_2 monolayers. Naively, one would expect the conduction band wave function to exponentially decay outside of the metallic layer. The spatial extent of the wave function is measured by scanning tunneling spectroscopy and is on the order of a nanometer. Since the PbSe layer is only 0.6 nm thick, the conduction bands of adjacent VSe_2 layers overlap within the PbSe. In this simple picture, the density of states of this overlapped region is 7500 times lower than the density of states within a VSe_2 layer. While this hypothesis needs to be tested by synthesizing heterostructures with thicker PbSe layers between VSe_2 layers, the ability to measure and subtract the lead and contact resistances from the total measured resistivity overcomes the inherent limitations of two lead resistance measurements in the cross-plane direction.

There are several experimental limitations to the approach presented herein to measure cross-plane resistivity, which depends on being able to extract top and bottom lead and contact resistances from contact end voltage measurements. This requires observing the contact end voltage increase as contacts are reduced in contact width, which depends on the ratio of the conductance of the contact to that of the sample. As the ratio increases, current crowding increases and lead contact width needs to be decreased to observe a voltage increase. Conversely, a reduced ratio requires thicker lead widths to obtain a contact end voltage dominated by the lead resistance. Since the conductance of the sample increases with sample thickness and different materials can be chosen to vary the contact conductance, there are some experimental parameters that can be tuned to optimize the experiment. However, samples with high in-plane resistances relative to the contact will be challenging to measure.

The second experimental factor to consider is sample thicknesses, which can often be adjusted to optimize the experiment. Thicker samples will increase the cross-plane sample resistance, increasing the percentage of the total cross-plane resistance caused by the sample. Increasing sample thickness will also, however, increase the broadening of the current path through the sample in the cross-plane measurement. To probe this factor, we simulated various conditions using the COMSOL Multiphysics software package as shown in Figure S2. Current broadening increases dramatically as sample thickness increases, but as sample thickness decreases, the electrical potential gradient change becomes limited to the near contact region. The lateral current profiles near the edges of contacts are similar to each other, which indicates that the current broadening effect is about the same across all the contacts with different contact widths. In this thickness regime, the graph of the material's cross-plane resistance versus contact width will approach zero much quicker than a $1/d$ dependence as a result of the current broadening. One can compensate for this factor by fitting the data to $1/(d + b)$, where b is the extent of the current broadening.

https://doi.org/10.1021/acsnano.3c13232
ACS Nano XXXX, XXX, XXX−XXX

Based on the discussion in the previous two paragraphs, the approach presented herein to measure cross-plane resistivity is best suited to anisotropic samples aligned such that the high resistivity direction is perpendicular to the sample substrate. High cross-plane resistivity for the material being examined allows film thickness to be kept small enough that current broadening is minimized and also results in a smaller percentage of the total measured cross-plane resistance due to the lead and contact resistances. Low in-plane resistivity enables current crowding to be measured with contact widths that can be prepared with optical lithography. Isotropic materials will be challenging to measure, as low resistivity materials will result in most of the total measured cross-plane resistance due to the lead and contact resistances. Subtracting two large numbers to obtain a small remainder leads to a large error in the remainder. High resistivity isotropic materials will require ultrathin contact widths to measure a change in the contact end voltage, as the current will concentrate at the beginning of the contact. Fortunately, there are many heterostructures where anisotropic behavior is expected. Another concern that arises is the possibility that the conduction behavior might be dominated by other mechanisms, such as tunneling and conductive filament (CF) formation through defects. In the future, we will verify the cross-plane conduction behavior by varying the film thicknesses and layer composition, as well as performing hysteresis measurements. Additionally, vdW monolayers and heterostructures have shown promising results in photochemical and photoelectrochemical reactions due to their high surface-to-volume ratio, strong photoabsorption, and intrinsically hosted catalytic sites.[46−48] While the catalytic performances in various reactions have been intensively studied, their conversion efficiencies also rely on charge carrier transport along both in-plane and cross-plane directions.[49,50] We believe our developed measurement technique will provide additional insights into future photocatalyst design.

CONCLUSION

In conclusion, we have fabricated and tested a facile method to measure the intrinsic cross-plane and in-plane resistivities of van der Waals heterostructures. By flowing current along the in-plane direction, the gold lead resistances and interface conductances of the top and bottom electrodes are first quantified by measuring the variation in current crowding as a function of contact width. The interface and lead resistances can then be subtracted from the total measured cross-plane resistance to obtain the cross-plane resistivity of the sample. We find that the in-plane and cross-plane contact resistances of the measured $(PbSe)_1(VSe_2)_1$ heterostructure differ by a factor of 7500. Within the temperature range from 6 to 300 K, the difference in the electric resistivity between the cross-plane and in-plane directions is temperature independent, suggesting that the cross-plane resistivity is due to overlap of the wave function of adjacent VSe_2 layers in the $(PbSe)_1(VSe_2)_1$ heterostructure. We also reported the observation of charge density wave transition in the cross-plane transport of $(PbSe)_1(VSe_2)_1$ heterostructure. We believe the developed framework of accurate characterization of in-plane and cross-plane resistivity, measured on the same sample, will be highly beneficial to the whole thin film research community.

METHOD

Device Fabrication. The device is fabricated by first patterning an array of five contact widths from 1 to 16 μm using electron beam lithography (Raith EBPG 5200) on oxidized Si substrates. Thirty nm thick Ti/Au is deposited on the pattern yielding a pattern of different width bottom contacts after liftoff. A second lithography step is used to define a rectangular window (600 μm × 40 μm) on the bottom electrodes. The material of interest is then deposited onto the patterned substrate. A second array of electrodes is then patterned to serve as top contacts aligned directly above the bottom contacts. To minimize sample heating during deposition of the top contacts, the substrates are approximately 1 m from the metal sources and the deposition rate is round 1 Å/s.

Heterostructure Synthesis and Characterization. Precursors were deposited on <100> Si wafers with native oxide using a custom-built physical deposition chamber. Elemental V (99.995%, Alfa Aesar) and Pb (99.8%, Alfa Aesar) were deposited using 6 keV electron beam guns while elemental Se (99.99%, Alfa Aesar) was deposited using a Knudsen effusion cell. Elemental layers were deposited by exposing the substrate to a plume of atoms from the heated sources. The time the substrate was exposed was controlled by pneumatic shutters that close after the desired thickness has been deposited. The desired thickness was measured using a quartz crystal microbalance and the sequence and thickness of elemental layers can be controlled using custom LabView software. The number of atoms of each element deposited was measured using X-ray fluorescence (XRF) using a Rigaku Primus II ZSX spectrometer. The measured XRF intensities were converted into the number of atoms per unit area for each constituent as described by Hamann and coworkers.[35] The period of the deposited sequence of layers was measured using X-ray reflectivity (XRR).

The precursors were converted to the targeted heterostructure by *ex situ* annealing at 300 °C for 30 min on a hot plate in an inert N_2 atmosphere (O_2 < 0.8 ppm). Specular X-ray diffraction (XRD), X-ray reflectivity (XRR) and grazing incidence in-plane X-ray diffraction (GIPXRD) patterns were collected using a Rigaku Smartlab diffractometer, also with Cu−Kα radiation (λ = 0.15418 nm). LeBail fitting of the GIPXRD data was performed on FullProf Suite to obtain lattice parameters. An FEI Titan G2 80−200 STEM with a Cs probe corrector and ChemiSTEM technology (X-FEG and Super-X EDS with four windowless silicon drift detectors) operated at 200 kV were used to obtain high-angle annular dark-field (HAADF) images and EDS scans over selected regions.

ASSOCIATED CONTENT

Supporting Information

The Supporting Information is available free of charge at https://pubs.acs.org/doi/10.1021/acsnano.3c13232.

Ohmic contact of all leads, current spreading simulation, contact end voltage drops at different temperatures, cross-plane resistivity times contact width d plotted as a function of d, material synthesis and device preparation, and linear plots of in-plane and cross-plane resistivity of the $(PbSe)_1(VSe_2)_1$ material (PDF)

https://doi.org/10.1021/acsnano.3c13232
ACS Nano XXXX, XXX, XXX−XXX

AUTHOR INFORMATION

Corresponding Authors

David C. Johnson − *Department of Chemistry, University of Oregon, Eugene, Oregon 97403, United States;* orcid.org/0000-0002-1118-0997; Email: davej@uoregon.edu

Stephen B. Cronin − *Ming Hsieh Department of Electrical Engineering, Department of Chemistry, and Department of Physics and Astronomy, University of Southern California, Los Angeles, California 90089, United States;* orcid.org/0000-0001-9153-7687; Email: scronin@usc.edu

Authors

Sizhe Weng − *Ming Hsieh Department of Electrical Engineering, University of Southern California, Los Angeles, California 90089, United States;* orcid.org/0000-0002-6555-2442

Yu Wang − *Mork Family Department of Chemical Engineering and Materials Science, University of Southern California, Los Angeles, California 90089, United States; Department of Mechanical Engineering, Stanford University, Stanford, California 94305, United States;* orcid.org/0000-0002-0307-1301

Celsey Price − *Department of Chemistry, University of Oregon, Eugene, Oregon 97403, United States*

Hannah R. Blackwood − *Department of Chemistry, University of Oregon, Eugene, Oregon 97403, United States;* orcid.org/0000-0003-2360-1119

Marisa Choffel − *Department of Chemistry, University of Oregon, Eugene, Oregon 97403, United States*

Aaron Miller − *Department of Chemistry, University of Oregon, Eugene, Oregon 97403, United States;* orcid.org/0000-0003-0493-9464

Ruoxi Li − *Mork Family Department of Chemical Engineering and Materials Science, University of Southern California, Los Angeles, California 90089, United States;* orcid.org/0000-0002-6432-6072

Mingrui Chen − *Mork Family Department of Chemical Engineering and Materials Science, University of Southern California, Los Angeles, California 90089, United States*

Ping Lu − *Sandia National Laboratories, Albuquerque, New Mexico 87185, United States*

Sina Ilkhani − *Department of Chemistry, University of Southern California, Los Angeles, California 90089, United States*

Arun Majumdar − *Department of Mechanical Engineering, Stanford University, Stanford, California 94305, United States;* orcid.org/0000-0003-4226-9705

Complete contact information is available at: https://pubs.acs.org/10.1021/acsnano.3c13232

Author Contributions

○S.W. and Y.W. contributed equally to this work. S.W., Y.W., D.C.J., and S.B.C. conceived and planned the experiments. S.W. carried out the experiment and analyzed the data and Y.W. derived the models and helped carry out the COMSOL simulations. C.P., H.R.B., M.C., and A.M. carried out the material synthesis and characterization. R.L. and M.C. assisted with device characterization and EBL. S.W., Y.W., D.C.J., and S.B.C. wrote the manuscript and all authors discussed the results and contributed to the final manuscript.

Notes

The authors declare no competing financial interest.

ACKNOWLEDGMENTS

This research was supported by the U.S. Department of Energy, Office of Basic Energy Sciences under Award No. DE-FG02-0746376 (Y.W.), the National Science Foundation (NSF) under Award No. CBET-2323031 (S.W.), and the Office of Naval Research Award N00014-22-1-2697 (R.L.). The research at the University of Oregon and Stanford University was supported by the Office of Naval Research MURI Award N00014-21-1-2377.

REFERENCES

(1) Geim, A. K.; Grigorieva, I. V. Van der Waals heterostructures. *Nature* **2013**, *499* (7459), 419−425.

(2) Haigh, S. J.; Gholinia, A.; Jalil, R.; Romani, S.; Britnell, L.; Elias, D. C.; Novoselov, K. S.; Ponomarenko, L. A.; Geim, A. K.; Gorbachev, R. Cross-sectional imaging of individual layers and buried interfaces of graphene-based heterostructures and superlattices. *Nat. Mater.* **2012**, *11* (9), 764−767.

(3) Venkatasubramanian, R.; Siivola, E.; Colpitts, T.; O'Quinn, B. Thin-film thermoelectric devices with high room-temperature figures of merit. *Nature* **2001**, *413* (6856), 597−602.

(4) Hamann, D. M.; Hadland, E. C.; Johnson, D. C. Heterostructures containing dichalcogenides-new materials with predictable nanoarchitectures and novel emergent properties. *Semicond. Sci. Technol.* **2017**, *32* (9), 093004.

(5) Silin, A. P. Semiconductor superlattices. *Sov. Phys. J.* **1985**, *28* (11), 972.

(6) Collier, C. P.; Vossmeyer, T.; Heath, J. R. NANOCRYSTAL SUPERLATTICES. *Annu. Rev. Phys. Chem.* **1998**, *49* (1), 371−404.

(7) Thompson, A. G. MOCVD technology for semiconductors. *Mater. Lett.* **1997**, *30* (4), 255−263.

(8) Ludowise, M. Metalorganic chemical vapor deposition of III-V semiconductors. *J. Appl. Phys.* **1985**, *58* (8), R31−R55.

(9) Liu, Y.; Weiss, N. O.; Duan, X.; Cheng, H.-C.; Huang, Y.; Duan, X. Van der Waals heterostructures and devices. *Nat. Rev. Mater.* **2016**, *1* (9), 16042.

(10) Cheng, R.; Wang, F.; Yin, L.; Wang, Z.; Wen, Y.; Shifa, T. A.; He, J. High-performance, multifunctional devices based on asymmetric van der Waals heterostructures. *Nat. Electron.* **2018**, *1* (6), 356−361.

(11) Hong, X.; Kim, J.; Shi, S.-F.; Zhang, Y.; Jin, C.; Sun, Y.; Tongay, S.; Wu, J.; Zhang, Y.; Wang, F. Ultrafast charge transfer in atomically thin MoS2/WS2 heterostructures. *Nat. Nanotechnol.* **2014**, *9* (9), 682−686.

(12) Yu, W. J.; Liu, Y.; Zhou, H.; Yin, A.; Li, Z.; Huang, Y.; Duan, X. Highly efficient gate-tunable photocurrent generation in vertical heterostructures of layered materials. *Nat. Nanotechnol.* **2013**, *8*, 952−958.

(13) Palacios-Berraquero, C.; Barbone, M.; Kara, D. M.; Chen, X.; Goykhman, I.; Yoon, D.; Ott, A. K.; Beitner, J.; Watanabe, K.; Taniguchi, T.; et al. Atomically thin quantum light-emitting diodes. *Nat. Commun.* **2016**, *7* (1), 12978.

(14) Britnell, L.; Gorbachev, R. V.; Jalil, R.; Belle, B. D.; Schedin, F.; Mishchenko, A.; Georgiou, T.; Katsnelson, M. I.; Eaves, L.; Morozov, S. V.; et al. Field-Effect Tunneling Transistor Based on Vertical Graphene Heterostructures. *Science* **2012**, *335* (6071), 947−950.

(15) Liu, Y.; Huang, Y.; Duan, X. Van der Waals integration before and beyond two-dimensional materials. *Nature* **2019**, *567* (7748), 323−333.

(16) Sarkar, D.; Xie, X.; Liu, W.; Cao, W.; Kang, J.; Gong, Y.; Kraemer, S.; Ajayan, P. M.; Banerjee, K. A subthermionic tunnel field-effect transistor with an atomically thin channel. *Nature* **2015**, *526* (7571), 91−95.

(17) Montgomery, H. C. Method for Measuring Electrical Resistivity of Anisotropic Materials. *J. Appl. Phys.* **1971**, *42* (7), 2971−2975.

(18) dos Santos, C. A. M.; de Campos, A.; da Luz, M. S.; White, B. D.; Neumeier, J. J.; de Lima, B. S.; Shigue, C. Y. Procedure for

measuring electrical resistivity of anisotropic materials: A revision of the Montgomery method. *J. Appl. Phys.* **2011**, *110* (8), 083703.
(19) Yang, B.; Liu, W. L.; Liu, J. L.; Wang, K. L.; Chen, G. Measurements of anisotropic thermoelectric properties in superlattices. *Appl. Phys. Lett.* **2002**, *81* (19), 3588−3590.
(20) Chen, J.; Hamann, D. M.; Choi, D. S.; Poudel, N.; Shen, L.; Shi, L.; Johnson, D. C.; Cronin, S. B. Enhanced Cross-plane Thermoelectric Transport of Rotationally-disordered $SnSe_2$ via Se Vapor Annealing. *Nano Lett.* **2018**, *18* (11), 6876−6881.
(21) Kwon, H.; Khan, A. I.; Perez, C.; Asheghi, M.; Pop, E.; Goodson, K. E. Uncovering thermal and electrical properties of Sb2Te3/GeTe superlattice films. *Nano Lett.* **2021**, *21* (14), 5984−5990.
(22) Ber, E.; Grady, R. W.; Pop, E.; Yalon, E. Uncovering the Different Components of Contact Resistance to Atomically Thin Semiconductors. *Adv. Electron. Mater.* **2023**, *9*, 2201342.
(23) Schroder, D. K. Contact Resistance and Schottky Barriers. In *Semiconductor Material and Device Characterization*; Wiley, 2005; pp. 127184.
(24) Najmaei, S.; Neupane, M. R.; Nichols, B. M.; Burke, R. A.; Mazzoni, A. L.; Chin, M. L.; Rhodes, D. A.; Balicas, L.; Franklin, A. D.; Dubey, M. Cross-Plane Carrier Transport in Van der Waals Layered Materials. *Small* **2018**, *14* (20), 1703808.
(25) Murrmann, H.; Widmann, D. Current crowding on metal contacts to planar devices. *IEEE Trans. Electron Devices* **1969**, *16* (12), 1022−1024.
(26) Schroder, D. K. *Semiconductor material and device characterization*; John Wiley & Sons, 2015.
(27) Berger, H. Solid State Electron. *Solid-State Electron* **1972**, *15*, 145.
(28) Wang, L.; Zhang, Z.-H.; Wang, N. Current crowding phenomenon: Theoretical and direct correlation with the efficiency droop of light emitting diodes by a modified ABC model. *IEEE J. Quantum Electron.* **2015**, *51* (5), 1−9.
(29) Yongsunthon, R.; Tao, C.; Rous, P.; Williams, E. Surface electromigration and current crowding. *Nanophenomena at Surfaces*; Springer, 2011, *47*, 113143. .
(30) Wang, Y.; Hamann, D. M.; Cordova, D. L. M.; Chen, J.; Wang, B.; Shen, L.; Cai, Z.; Shi, H.; Karapetrova, E.; Aravind, I.; et al. Enhanced Low-Temperature Thermoelectric Performance in $(PbSe)_{1+\delta}(VSe_2)_1$ Heterostructures due to Highly Correlated Electrons in Charge Density Waves. *Nano Lett.* **2020**, *20* (11), 8008−8014.
(31) Hite, O. K.; Falmbigl, M.; Alemayehu, M. B.; Esters, M.; Wood, S. R.; Johnson, D. C. Charge density wave transition in (PbSe) 1+ δ (VSe2) n compounds with n= 1, 2, and 3. *Chem. Mater.* **2017**, *29* (13), 5646−5653.
(32) Cordova, D. L. M.; Fender, S. S.; Kam, T. M.; Seyd, J.; Albrecht, M.; Lu, P.; Fischer, R.; Johnson, D. C. Designed synthesis and structure−property relationships of kinetically stable [(PbSe) 1+ δ] m (VSe2) 1 (m= 1, 2, 3, 4) heterostructures. *Chem. Mater.* **2019**, *31* (20), 8473−8483.
(33) Falmbigl, M.; Putzky, D.; Ditto, J.; Esters, M.; Bauers, S. R.; Ronning, F.; Johnson, D. C. Influence of defects on the charge density wave of ([SnSe] 1+ δ) 1 (VSe2) 1 ferecrystals. *ACS Nano* **2015**, *9* (8), 8440−8448.
(34) Berger, H. Contact resistance on diffused resistors. In *1969 IEEE International Solid-State Circuits Conference. Digest of Technical Papers*, IEEE, 1969..
(35) Wang, Y.; Hamann, D. M.; Cordova, D. L. M.; Chen, J.; Wang, B.; Shen, L.; Cai, Z.; Shi, H.; Karapetrova, E.; Aravind, I.; et al. Enhanced Low-Temperature Thermoelectric Performance in $(PbSe)_{1+\delta}(VSe_2)_1$ Heterostructures due to Highly Correlated Electrons in Charge Density Waves. *Nano Lett.* **2020**, *20* (11), 8008−8014.
(36) Ting, C.-Y.; Chen, C. Y. A study of the contacts of a diffused resistor. *Solid-State Electron* **1971**, *14* (6), 433−438.
(37) Scorzoni, A.; Finetti, M. Metal/semiconductor contact resistivity and its determination from contact resistance measurements. *Mater. Sci. Rep.* **1988**, *3* (2), 79−137.
(38) Moon, I.; Choi, M. S.; Lee, S.; Nipane, A.; Hone, J.; Yoo, W. J. Analytical measurements of contact resistivity in two-dimensional WSe2 field-effect transistors. *2D Mater.* **2021**, *8* (4), 045019.
(39) Sambles, J. R.; Elsom, K. C.; Jarvis, D. J. The electrical resistivity of gold films. *Philos. Trans. R. Soc., A* **1982**, *304* (1486), 365−396.
(40) De Vries, J. Temperature and thickness dependence of the resistivity of thin polycrystalline aluminium, cobalt, nickel, palladium, silver and gold films. *Thin Solid Films* **1988**, *167* (1−2), 25−32.
(41) Vaziriserehk, M. R.; Sumaiya, S. A.; Martini, A.; Baykara, M. Z. Measurement of electrical contact resistance at nanoscale gold-graphite interfaces. *Appl. Phys. Lett.* **2019**, *115* (9), 091602.
(42) Matsubara, K.; Sugihara, K.; Tsuzuku, T. Electrical resistance in the c direction of graphite. *Phys. Rev. B* **1990**, *41* (2), 969−974.
(43) Peng, H.; Xie, C.; Schoen, D. T.; Cui, Y. Large Anisotropy of Electrical Properties in Layer-Structured In2Se3 Nanowires. *Nano Lett.* **2008**, *8* (5), 1511−1516.
(44) Cao, W.; Huang, M.; Yeh, C.-H.; Parto, K.; Banerjee, K. Impact of transport anisotropy on the performance of van der Waals materials-based electron devices. *IEEE Trans. Electron Devices* **2020**, *67* (3), 1310−1316.
(45) Wiegers, A. G. Misfit layer compounds: Structures and physical properties. *Prog. Solid State Chem.* **1996**, *24* (1−2), 1−139.
(46) Li, Y.; Gao, C.; Long, R.; Xiong, Y. Photocatalyst design based on two-dimensional materials. *Mater. Today Chem.* **2019**, *11*, 197−216.
(47) Chen, J.; Bailey, C. S.; Hong, Y.; Wang, L.; Cai, Z.; Shen, L.; Hou, B.; Wang, Y.; Shi, H.; Sambur, J.; et al. Plasmon-Resonant Enhancement of Photocatalysis on Monolayer WSe2. *ACS Photonics* **2019**, *6* (3), 787−792.
(48) Jun, S. E.; Lee, J. K.; Jang, H. W. Two-dimensional materials for photoelectrochemical water splitting. *Energy Adv.* **2023**, *2* (1), 34−53.
(49) Chen, J.; Bailey, C. S.; Cui, D.; Wang, Y.; Wang, B.; Shi, H.; Cai, Z.; Pop, E.; Zhou, C.; Cronin, S. B. Stacking Independence and Resonant Interlayer Excitation of Monolayer WSe2/MoSe2 Heterostructures for Photocatalytic Energy Conversion. *ACS Appl. Nano Mater.* **2020**, *3* (2), 1175−1181.
(50) Lin, Y.-R.; Cheng, W.-H.; Richter, M. H.; DuChene, J. S.; Peterson, E. A.; Went, C. M.; Al Balushi, Z. Y.; Jariwala, D.; Neaton, J. B.; Chen, L.-C.; et al. Band Edge Tailoring in Few-Layer Two-Dimensional Molybdenum Sulfide/Selenide Alloys. *J. Phys. Chem. C* **2020**, *124* (42), 22893−22902.

https://doi.org/10.1021/acsnano.3c13232
ACS Nano XXXX, XXX, XXX−XXX